ELSEVIER

Earth and Planetary Science Letters 198 (2002) 129–145

EPSL

www.elsevier.com/locate/epsl

Inversion of body-wave delay times for mantle structure beneath the Hawaiian islands: results from the PELENET experiment

Cecily J. Wolfe [a,*], Sean C. Solomon [b], Paul G. Silver [b], John C. VanDecar [b], Raymond M. Russo [c]

[a] *Hawaii Institute of Geophysics and Planetology, University of Hawaii at Manoa, Honolulu, HI 96822, USA*
[b] *Department of Terrestrial Magnetism, Carnegie Institution of Washington, Washington, DC 20015, USA*
[c] *Department of Geological Sciences, Northwestern University, Evanston, IL 60208, USA*

Received 11 October 2001; received in revised form 23 January 2002; accepted 25 January 2002

Abstract

As an experiment to assess the nature of resolvable seismic velocity anomalies in the mantle surrounding the Hawaiian Islands, we operated a temporary network – known as PELENET – consisting of seven broadband portable seismometers on the islands of Kauai, Molokai, Maui, and Hawaii during 1995–1999. Here we report the inversion of body-wave delay times across the network, including arrivals at the Global Seismic Network station KIP on Oahu and the Ocean Seismic Network Pilot Experiment south of Oahu, to determine the three-dimensional seismic velocity structure of the upper mantle of the region. The consistent feature observed in both P- and S-wave inversions is a low-velocity anomaly beneath Maui and Molokai, which we suggest may reflect a zone of secondary melting in the asthenosphere downstream from the hotspot locus. The inversions do not resolve a cylindrical low-velocity plume in the upper mantle beneath the island of Hawaii, but resolution tests indicate that this outcome could be the result of the sparse and nearly linear distribution of stations combined with the incomplete azimuthal coverage of earthquake sources. A determination of the detailed three-dimensional structure of the upper mantle beneath the Hawaiian hotspot will require a simultaneous deployment of both ocean-bottom and land seismometers.

Keywords: Hawaii; hot spots; mantle plumes; tomography

1. Introduction

A number of oceanic hotspots are believed to be the surface manifestations of plumes of hot, upwelling mantle material, but the characteristics of this mantle flow have remained enigmatic. While the pattern of upper mantle flow and its interaction with the lithosphere can be expected to have a strong influence on such geophysical observables as topography, gravity, and heat flow (e.g., [1–7]), as well as on the chemistry and petrology of ocean island basalts (e.g., [8]), the dynamics of these processes are not well

* Corresponding author. Tel.: +1-808-956-6347; Fax: +1-808-956-3188.
E-mail address: cecily@soest.hawaii.edu (C.J. Wolfe).

0012-821X/02/$ – see front matter
PII: S0012-821X(02)00493-4

understood. Hawaii, which is calculated to have the largest buoyancy flux of all active plumes [4], is one of the most thoroughly studied hotspots in the world, yet there remain fundamental geodynamic questions regarding the nature of mantle flow and plume–lithosphere interaction in the region. For example, it is not known whether the topographic swell is generated by thermal erosion of the lithosphere [1,2], flow of hot, buoyant plume material in the asthenosphere (e.g., [3,5,9]), or buoyancy of a depleted mantle residue from plume melting [7,10]. The location, radius, temperature anomaly, and depth extent of the Hawaiian mantle plume are all poorly constrained.

Global mantle tomography and large-scale regional seismic models do not have sufficient resolution to image reliably small-scale features such as mantle plumes, which have horizontal dimensions of a few hundred kilometers or less and are not illuminated by the presence of local deep earthquake sources, as in the case of slabs. In contrast, seismological data from regional arrays of broadband, three-component instruments provide a means for resolving the detailed characteristics of upper mantle seismic structure beneath hotspots at wavelengths of ~20–500 km, as is necessary for constraining geodynamic models.

Several seismic studies in the Hawaiian region have characterized aspects of local mantle structure. Inversions of short-period teleseismic P-wave delays on the island of Hawaii have yielded images of low-velocity anomalies in the lithosphere, which have been taken to indicate the presence of melt migrating upward to the active volcanoes [11,12]. Measurements of Rayleigh wave dispersion have been carried out with land-based stations [13,14] and with differential pressure gauges on the seafloor [15] to assess the presence of hot asthenosphere emanating from the plume and the degree of downstream lithospheric erosion. Mantle discontinuities beneath the islands have been mapped using receiver functions [16]. While the results of these analyses have been promising, the limited distribution of stations in these experiments has left open the full nature of the mantle seismic structure beneath the Hawaiian hotspot.

The ICEMELT experiment in Iceland [17] illustrated that body-wave data from a temporary seismic network centered over a hotspot can resolve the characteristic features of a mantle plume. The delay times of teleseismic body waves at ICEMELT from a good distribution of back azimuths were inverted to image the three-dimensional P- and S-wave velocity of the upper mantle between depths of 100 and 400 km. The most prominent feature imaged is an approximately cylindrical low-velocity anomaly beneath central Iceland extending throughout the model region and inferred to represent the locus of the hot, upwelling Iceland mantle plume [18]. P to S conversions from upper mantle discontinuities beneath Iceland show that the mantle transition zone beneath central and southern Iceland is thinned, consistent with the hypothesis that the mantle plume originates from deeper than 700 km [19]. Data from a larger deployment of broadband seismometers in Iceland subsequent to ICEMELT are expected to provide additional resolution of the Iceland plume [20,21].

Here we report the results from an experiment to determine the seismic velocity structure of the upper mantle beneath the region of the Hawaiian Islands from the relative arrival times of body waves from teleseismic earthquakes. The experiment, termed PELENET, involved the deployment of seven broadband portable seismometers along the island chain from Hawaii to Kauai. The principal objective of the experiment was to assess the nature of mantle seismic velocity anomalies in the Hawaiian region as a precursor to a larger deployment of both ocean-bottom and land seismometers.

2. The PELENET seismic network

The PELENET experiment (Fig. 1) consisted of seven three-component STS-2 seismometers equipped with REFTEK recorders and deployed on the islands of Kauai, Molokai, Maui, and Hawaii. Contemporary data were also available from the Global Seismic Network (GSN) station KIP on Oahu and from the Ocean Seismic Network Pilot Experiment (OSNPE) [22] at the seafloor 225 km southwest of Oahu (Fig. 1). Four of the

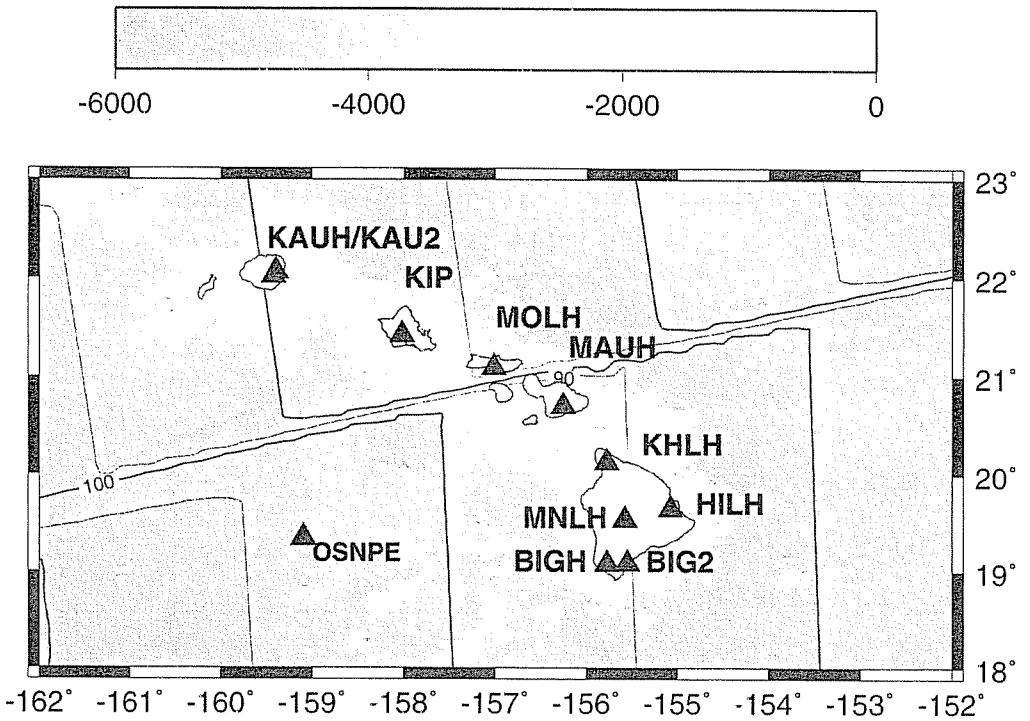

Fig. 1. Locations of seismometers used in the PELENET experiment. Bathymetry (in m) around the Hawaiian Islands is from Smith and Sandwell [35]. Contours of seafloor age (10-Myr contour interval) are from Mueller et al. [36]. Note the offset in age across the Molokai Fracture Zone. See text for additional information.

PELENET instruments (KAUH/KAU2, MAUH, MOLH, and BIGH/BIG2) were deployed and operated by the Carnegie Institution of Washington (CIW) between December 1995 and September 1999. Three stations (HILH, KHLH, and MNLH) were installed and operated by Northwestern University; the data used in this paper from those stations span the period July 1998 to March 1999. Two of the stations were moved during the experiment: station BIGH was operated from December 1995 to July 1996, but this instrument was subsequently moved to a quieter site farther inland at BIG2. Station KAUH operated from December 1995 to August 1998, but the instrument was subsequently moved to KAU2.

Stations were serviced every 3 months to download data and to correct any problems discovered. During service rounds it was sometimes found that one or more seismometers malfunctioned for some reason (e.g., seismometer mass off center, power problems, cable problems). The log files also revealed some intervals during which the GPS clocks did not lock; data from such periods were not used for the delay-time analyses. We used no arrivals from station KHLH, because both timing and recording problems severely reduced the set of useful data.

The OSNPE was carried out at Ocean Drilling Program hole 843B from late January to early June 1998 [22]. The seismometers included in the experiment were a Teledyne Geotech KS-54000 deployed 242.5 m beneath the seafloor in a borehole, a Guralp CMG-3T deployed on the seafloor, and a Guralp CMG-3T buried in sediments just beneath the seafloor. Because of timing problems with the OSNPE seafloor or buried instruments, we used only the borehole data for delay-time measurements. The seafloor instrument was nonetheless important for assessing the detectability and quality of body waves potentially recordable by a temporary array of ocean-bottom seismometers similar in design to the network deployed in the MELT experiment [23].

3. Body-wave delay-time measurements

The relative delay times of filtered P and S

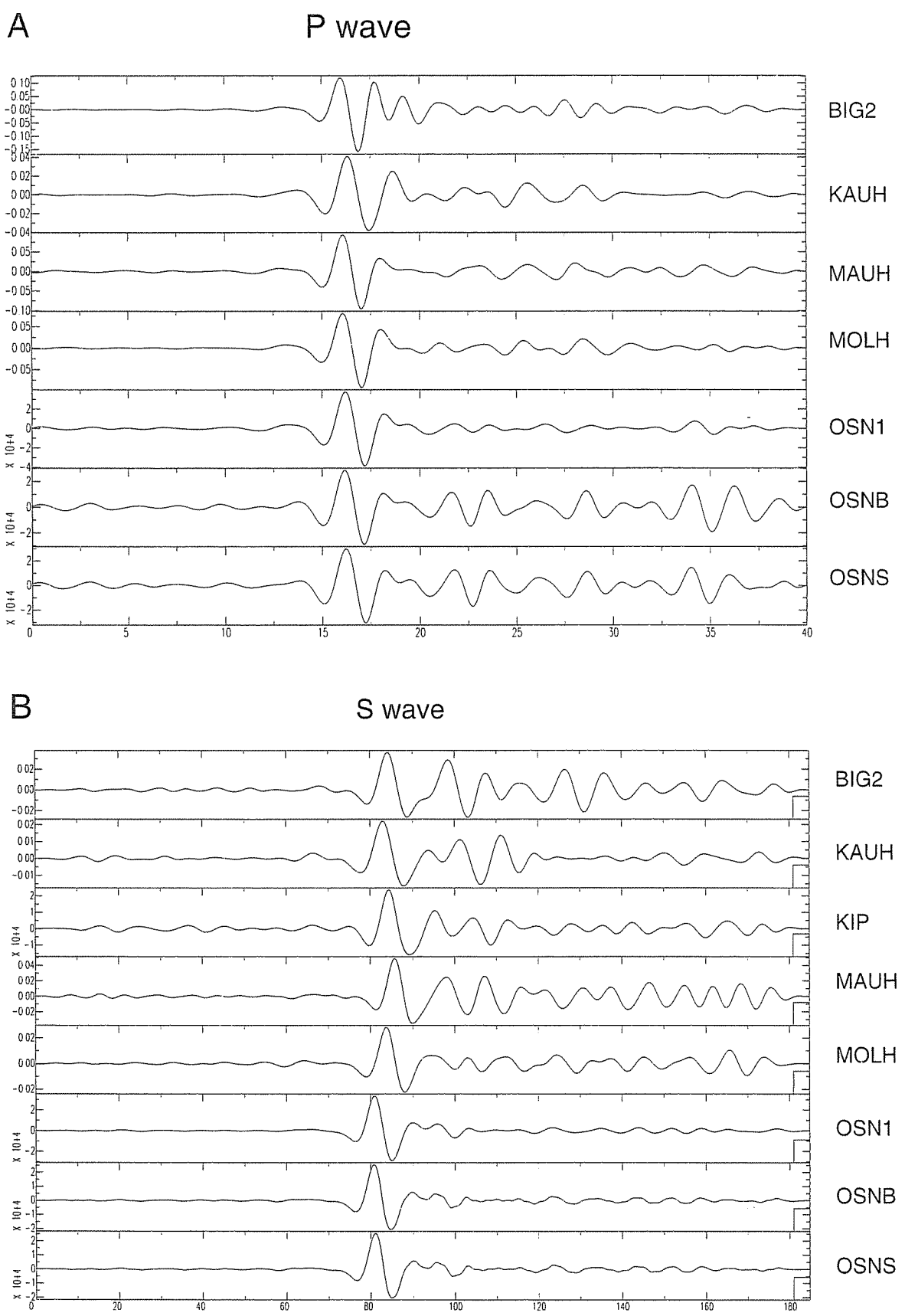
A
P wave
BIG2
KAUH
MAUH
MOLH
OSN1
OSNB
OSNS
B
S wave
BIG2
KAUH
KIP
MAUH
MOLH
OSN1
OSNB
OSNS

Fig. 2. Filtered seismograms of PELENET data. (A) P waves recorded from an M_b 6.5 earthquake that occurred on March 29, 1998, at 43° distance from PELENET. (B) S waves recorded from an M_b 6.1 earthquake that occurred on May 16, 1998, at 47° distance from PELENET. Both events were from the Tonga region. Station names are as in Fig. 1. OSNPE data are from the borehole (OSN1), the seafloor (OSNS), and the buried seismometer (OSNB).
←

waves from earthquakes were measured with the multichannel cross-correlation technique of VanDecar and Crosson [24]. Only earthquakes that yielded at least four arrival times for a given phase were included. To minimize nonlinear effects in the tomography, we used earthquakes only at teleseismic distances (angular distances greater than 30°) so that no wave paths bottomed within the steep gradients of the Earth's transition zone above 660 km depth. Waveforms of P waves bandpass filtered within 0.5–2 Hz and S waves filtered within 0.05–0.1 Hz are well correlated across the network (Fig. 2). The resulting set of delay times is of high accuracy. The average standard error obtained from the method of VanDecar and Crosson [24] is 5 ms for P waves and 15 ms for S waves. However, these values are judged to be too small, and instead we prefer standard errors of about 20 ms for P waves and 100 ms for S waves, similar to the errors found for data at Iceland [18] and Brazil [25]. We do not correct for the different instrument responses, but simulations in which delay times were determined from both corrected and uncorrected waveforms indicate that the instrument response differences are not significant for this study.

Microseismic noise at the Hawaiian Islands, which lie in one of the noisiest areas in the Pacific Ocean [26], reduces the detectability of teleseismic waves. The sparsity of the PELENET network also reduced the number of events. Because we invert for velocity structure and earthquake hypocentral relocations, at least four arrivals were required for an earthquake to be included in the delay-time inversion, so a number of earthquakes were discarded at times when the network was not fully operational or because a few stations had higher noise levels. A larger seismic network would increase the frequency of earthquakes for which delay times could be utilized.

The distribution of earthquakes for which relative arrival times were obtained within the frequency bands chosen for tomographic inversion is shown in Fig. 3. Direct P phases were from events at distances of 35–85°; direct S phases were from events at 35–80°; SKSac phases were from distances of 95–110°; no pickable PKP phases were obtained. The azimuthal distribution of earthquakes is not complete. The coverage of arrivals is good from about 200° to 360° azimuth, with earthquakes from subduction zones in the north, west, and south Pacific providing excellent sources for body waves. Coverage is poor to the east, however, where most arrivals are limited in azimuth from about 80° to 100° for direct P and S phases from earthquakes at the Central American subduction zone; SKS phases are also observed from South American earthquakes. Earthquakes from western North America and the southern East Pacific Rise and Pacific–Antarctic ridge rarely produce pickable body waves at PELENET. The sets of earthquakes that yielded P- and S-wave delays differ. Of the 82 earthquakes that yielded S phases and the 63 earthquakes that yielded P phases, only 28 earthquakes produced both measurable P- and S-wave arrivals in the frequency bands of interest.

Also of interest for future seafloor observations in the region are the number of measurable body-wave arrivals at the OSNPE. During the 3-month OSNPE deployment, we obtained 15 picks for S waves (both direct S and SKSac). The detectability on the seafloor instrument for S waves was equivalent to that found for the borehole instrument, with 19 pickable S waves observed (the recording dates for the borehole and seafloor instruments differed slightly). The detectability was less for P waves, as expected given the higher noise levels at 1-s period [22]. We obtained 12 picks for P waves on the borehole instrument, which was equivalent to the detectability at the island stations. Of these picks, six were of good quality on the seafloor instrument, and a separate event, which was not included due to problems with the

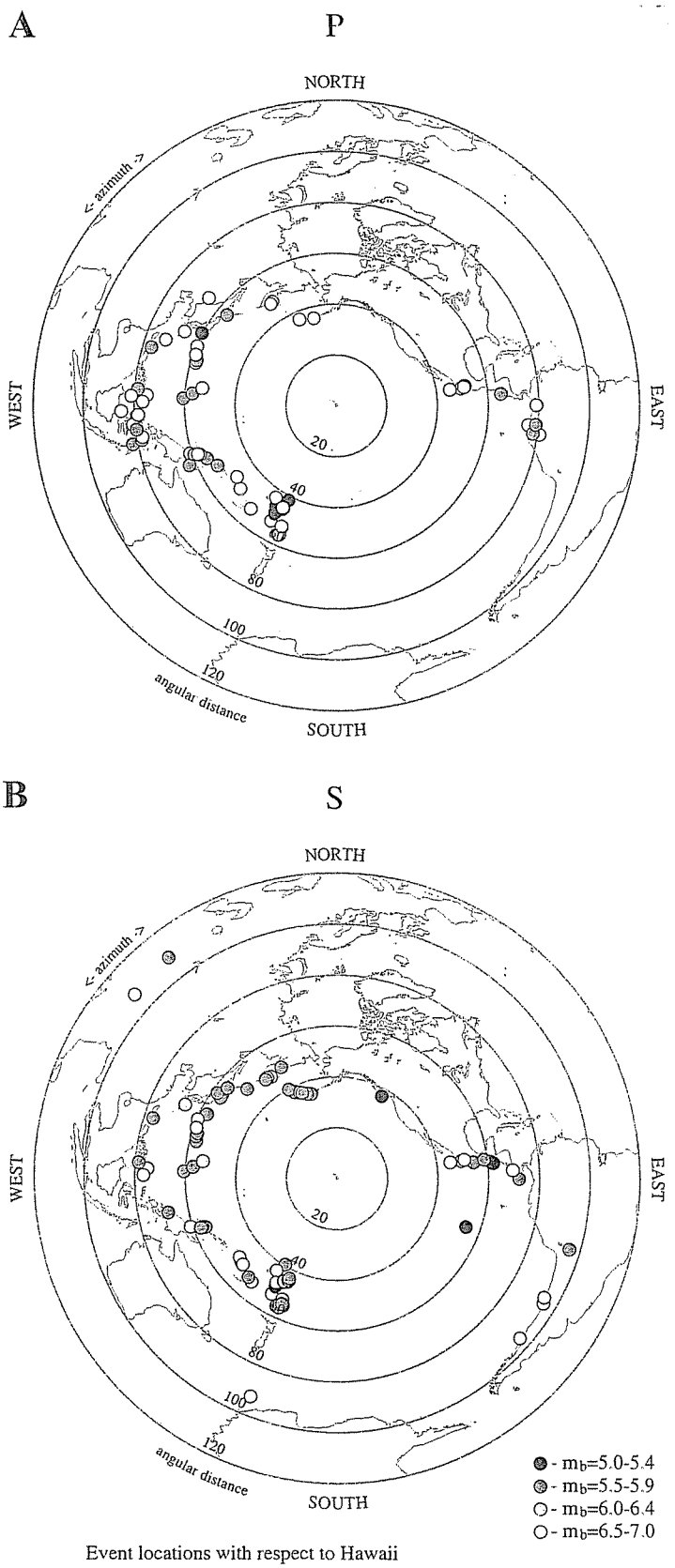

Fig. 3. Locations of earthquakes used in the delay-time inversions. (A) Earthquakes used in the P-wave delay-time inversions. (B) Earthquakes used in the S-wave delay-time inversions. Direct S waves are used for distances of 30–80°, and SKSac phases are used for 95–110°.

land stations, was also pickable, giving a total of seven good P waves on the seafloor instrument. Another seven earthquakes, including four not included in the delay-time inversion, would be considered of questionable use, where a P phase was evident but it was uncertain whether the data could yield a reliable pick. Our results are similar to those of Collins et al. [22] and suggest that a deployment of ocean-bottom seismometers around Hawaii will record earthquakes yielding S phases at a rate similar to that observed at PELENET but that the rates of earthquakes yielding P phases will be reduced from those at land stations by perhaps 50%.

4. Tomographic inversion for mantle structure

P- and S-wave delays have been independently inverted for three-dimensional velocity structure, earthquake relocations, and station terms by the method of VanDecar et al. [25]. Variations in structure are parameterized by splines under tension constrained at a series of regular knots. We used 32 knots in depth, 33 knots in latitude, and 41 knots in longitude. The grid extends from 0 to 1000 km in depth, 15–26° in latitude, and −164° to −151° in longitude. Within the region of appreciable resolution, the knots are spaced at 25 km in depth and 0.25° in latitude and longitude. Because such inversions are inherently underdetermined, we choose to search for the minimum-structure model required to satisfy the data by minimizing spatial gradients and roughness implemented through first- and second-difference operators. The system is inverted with a conjugate-gradients procedure iterated to convergence. The method also iterates on these inversions, systematically down-weighting equations associated with outlying residuals from the previous iteration. While the inversion scheme allows iterations to incorporate the nonlinear effects from three-dimensional ray tracing, the limited resolution of structure by PELENET data does not justify this procedure, and we report linear inversions only in this paper.

The inversions incorporate relative arrival times of 286 P waves from 63 earthquakes and 373 S wave times from 82 earthquakes. The dominant seismic wavelengths are ~10 km for the P waves and 50–75 km for the S waves. The inversion solutions are shown in Fig. 4 as percent velocity perturbations to a standard radial Earth model [27]; only the interior region, where appreciable resolution is expected to be obtained, is plotted. Our models account for 96% of the root-mean-squared (rms) residual for P-wave delay data (from 0.45 to 0.02 s) and 90% of the rms residual for S-wave delay data (from 1.1 to 0.1 s).

Because the station spacing varies from 50 to 200 km and incidence angles of teleseismic waves steepen in the shallowmost mantle, there are no crossing wave paths above about 100 km depth. Velocity structure is thus poorly constrained at these shallow depths, although the station terms shown in Fig. 4 account in part for the integrated differences in mantle structure above 100 km depth, combined with the effects of crustal thickness variations and differences in station elevation. Subtracting the station terms from the delay times reduces the rms from 0.45 to 0.17 s for P waves and from 1.1 to 0.62 s for S waves; these corrected residuals more accurately reflect the magnitude of delay-time anomalies that will be mapped into three-dimensional velocity structure. Large negative station terms, −1.1 s for P models and −3.0 s for S models, are obtained at the OSNPE site, much of which likely reflects the lower elevation (4.4 km below sea level) and thinner crust at this site than at the island stations. For example, with a station at sea level on 15-km-thick crust having a crustal P-wave velocity of 6.0 km/s and underlain by mantle of velocity 8.0 km/s, and a seafloor station at 4.4 km depth on 6-km-thick crust, this geometry would produce at the seafloor site about a −0.9 s relative delay for P waves and a −1.7 s delay for S waves for a V_P/V_S ratio of 1.8.

Neither the nearly linear distribution of stations (Fig. 1) nor the incomplete azimuthal coverage of earthquakes (Fig. 3) is ideal for constraining three-dimensional velocity models. These limitations degrade the resolution of the final images, and care should be taken when interpreting the results (Fig. 4). The consistent feature in both P- and S-wave models is a low-velocity anomaly

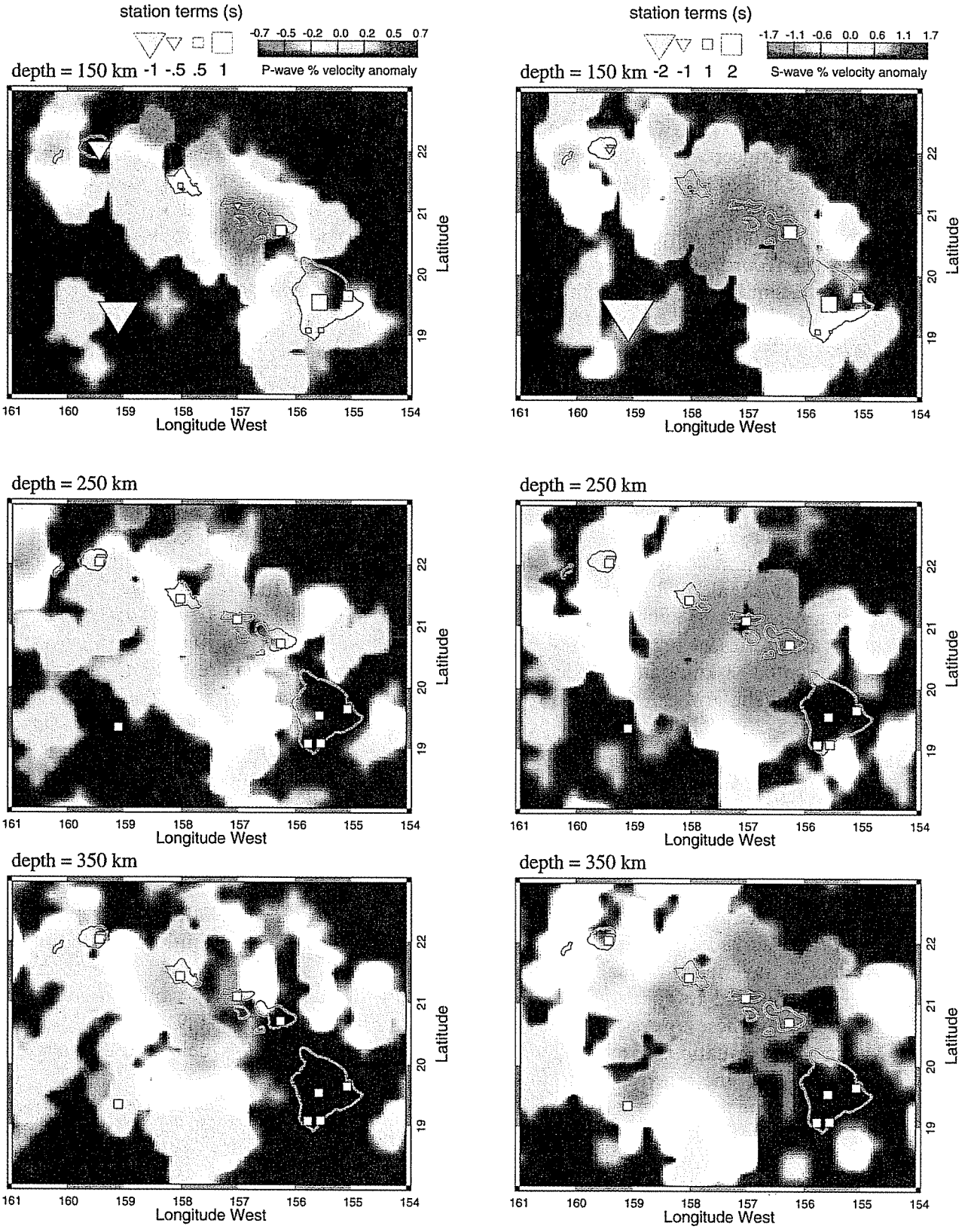
station terms (s)
-0.7 -0.5 -0.2 0.0 0.2 0.5 0.7
P-wave % velocity anomaly
depth = 150 km -1 -.5 .5 1
depth = 250 km
depth = 350 km
Latitude
Longitude West
161 160 159 158 157 156 155 154
19 20 21 22
station terms (s)
-1.7 -1.1 -0.6 0.0 0.6 1.1 1.7
S-wave % velocity anomaly
depth = 150 km -2 -1 1 2
depth = 250 km
depth = 350 km
P-wave model
S-wave model

Fig. 4. Cross-sections through the P-wave (left-hand column) and S-wave (right-hand column) models. Velocity perturbation models are shown in map view at depths of 125 km (top row), 250 km (middle row), and 350 km (bottom row). The velocity perturbations are relative variations across the modeled volume; the absolute velocities are unconstrained. Yellow-to-red colors represent low-velocity anomalies; regions with sparse coverage are faded to black. Station locations are shown as white squares in the middle row. Square and triangular symbols in the top row indicate the magnitude and sign of the station terms. The inversions solve simultaneously for independent (undamped) station terms to absorb as much shallow structure as possible into these terms and to avoid projecting such structure into the underlying velocity model. These station-term times represent the vertical travel time of waves associated with each station and thus account in part for the integrated differences in mantle structure above about 100 km depth, combined with the effects of crustal thickness variations and differences in station elevation. The coastlines of the Hawaiian Islands are shown as black lines.
←

in the upper mantle beneath the vicinity of Maui and Molokai. The maximum magnitude of the anomaly is about 0.6% for P-wave models and 1.8% for S-wave models. We conducted a series of tests to assess the robustness of this result, by varying the range of smoothing values, by limiting the depth extent of the model, and by not solving for earthquake relocations. The low velocities beneath Maui and Molokai are always present in the solution, although the amplitude of the anomaly decreases for inversions constrained to yield smoother models, the amplitude of the anomaly increases for inversions in which variations are constrained to shallower depths, and secondary structures can appear for depth-constrained models or models without earthquake relocations. Since we interpret only features that are consistent across a range of smoothing parameters, and since we calibrate the degree of amplitude reduction with the use of resolution tests, the choice of specific smoothing parameters will have little influence on the conclusions presented here.

The depth extent, magnitude, and shape of the anomaly at Maui and Molokai are not well constrained. For example, we have conducted a number of inversions where models were 'squeezed' to allow structure only within a particular depth interval (Fig. 5). For squeezed models, some of the structure may be mapped into earthquake relocations, so we plot both the rms delay-time residual and the rms of earthquake relocations. We find that models squeezed to allow only shallow structure (above 100 km depth) do not fit the data well, giving a large rms residual and also forcing large earthquake relocations. Models with less severe squeezing (structure only above 200, 300, 400, 500, 700, and 1000 km) consistently reduce the rms residual and rms earthquake relocations. However, models squeezed to various 100-km depth intervals (100–200, 200–300, 300–400, 400–500, and 500–600 km) all give similar rms residuals, showing that the data are equally sensitive to these different depth intervals.

A better understanding of the data limitations can be gathered by examining the geometry of the ray set. Horizontal projections of the rays in the depth intervals 0–100, 100–200, 200–300, and 300–400 km are shown in Fig. 6. The spatial coverage of rays varies strongly across the model region, which leads to spatial aliasing in the models. For example, coverage around the island of Hawaii is poor in the depth interval 100–400 km. Fig. 6 also illustrates how the model region is not well sampled by crossing rays, so anomalies may be smeared upward or downward along individual rays and are not well constrained in depth.

5. Resolution tests

We conducted several resolution tests in which a known synthetic anomaly is used to calculate synthetic travel times with the PELENET ray sets, Gaussian noise (rms of 50 ms for P waves and 100 ms for S waves) is added, and the synthetic data are inverted. As a synthetic model for the Maui–Molokai anomaly, we consider a vertical cylinder having a low-velocity anomaly with a radius in map view of 75 km (defined by the radial distance at which the perturbation drops below 1/e of the maximum) and a maximum amplitude of 2% in the depth interval 100–200 km. Structure is assumed to decay exponentially with

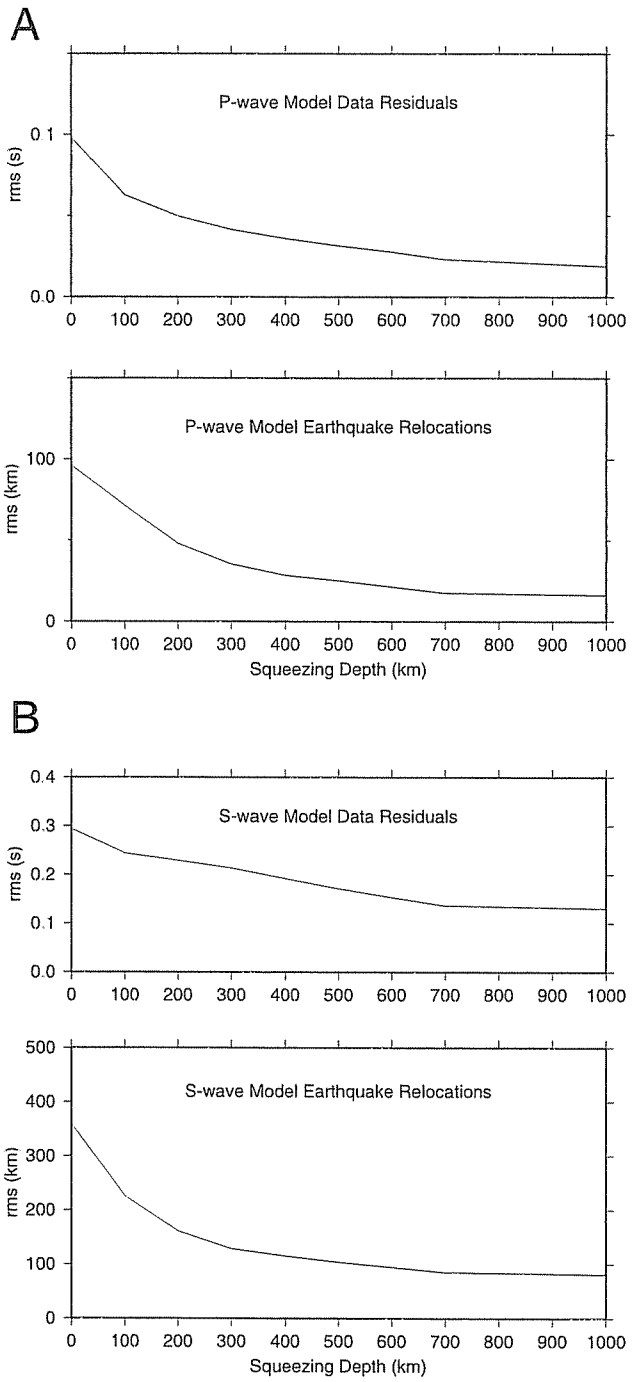

Fig. 5. Rms delay-time residual and rms earthquake relocations for depth-constrained models. The horizontal axis indicates the squeezing depth, i.e., the deepest level of allowed model variations (model values below this depth are forced to small values by heavy damping in this region). For shallow squeezing depths, the models map delay-time anomalies caused by upper mantle structure into more extreme earthquake relocations. While the method of VanDecar et al. [25] iterates on inversions, systematically down-weighting equations associated with outlying residuals from the previous iteration, we did not incorporate downweighting in these tests. (A) P-wave model values. (B) S-wave model values.

vertical distance above 100 km and below 200 km; the scale length for exponential decay is taken to be 75 km. Resolution tests for such a model (e.g., Fig. 7) show that the magnitude of a low-velocity anomaly beneath Maui–Molokai would be reduced by a factor of two to three in the delay-time inversions and that vertical smearing will occur.

Our solutions do not image a cylindrical low-velocity anomaly beneath Hawaii, as would be expected for a hot, upwelling plume. Such an anomaly, however, would not be recovered by our inversion because of the poor ray coverage beneath Hawaii (Fig. 6), which is due to the limited distribution of island stations and earthquake sources. To sample adequately the hypothesized plume in the upper mantle beneath Hawaii would require that the body-wave arrivals be recorded by a network of ocean-bottom seismometers surrounding Hawaii as well as by land stations. In particular, rays undershooting the island of Hawaii are needed to cross the plume conduit in the depth interval 100–400 km.

In order to further quantify why the hypothesized plume conduit would be poorly resolved by PELENET, we conducted two additional types of resolution tests for both the P-wave and the S-wave ray sets. First, resolution tests were performed using a vertical-cylinder low-velocity anomaly with a Gaussian profile 75 km in radius in map view, a maximum anomaly of 2%, and a depth extent of 150–600 km, with exponentially decaying structure above and below as described previously. The anomaly is taken to be centered at 19.3°N, −155.5°E, where Hauri [28] predicts the Hawaiian plume locus. For this geometry, PELENET has poor resolution of the plume structure, reducing the magnitude of the anomaly by a factor of about five. Adding to this synthetic model the shallow synthetic low-velocity anomaly beneath Maui and Molokai further degrades the resolution of the Hawaiian structure. A test with the two superposed synthetic models yields an image where the dominant structure is the Maui–Molokai feature and the structure at Hawaii is of low amplitude. Li et al. [16], on the basis of receiver functions, suggest that the Hawaiian plume conduit is located to the south-southwest

of Hawaii at the depth of the mantle transition zone but beneath Hawaii at depths of 130–140 km. We therefore tested the resolution of models of a tilted plume conduit linearly sloping to the south-southwest with depth, but this geometry would also not be well imaged by PELENET data.

Resolution tests have also been performed with the temperature and melt-depletion fields calculated by the geodynamic model of Ribe and Christensen [6] for the depths 0–400 km. While melt production is calculated in these models, the distribution of melt is not estimated, so the effect of melt is not included in these tests. The tests indicate that PELENET delay-time inversions will be insensitive to the depletion field calculated by Ribe and Christensen [6], for an increase in velocity by 0.1% per 1% increase in depletion [29], with the insensitivity reflecting the fact that the predicted velocity anomalies are small ($\sim$1%), vary over a broad length scale, and occur in a thin layer at depths $\sim$75–125 km in the mantle where ray paths do not cross. We consider a range of factors to convert temperature anomaly to velocity. A minimum-anomaly model is taken by assuming a decrease in velocity of 1% per 160°C temperature anomaly [29], a value derived from laboratory measurements. A maximum-anomaly model is taken by assuming a decrease in velocity of 1% per 100°C for P waves and per 75°C for S waves, values that approximate the effect of anelasticity on the partial derivatives given by Karato [30].

A resolution test on the Ribe and Christensen [6] temperature field for the S-wave model using the Karato-type conversion factor is illustrated in Fig. 8. The geodynamic model contains the following important features: the upwelling plume is characterized by a cylindrical low-velocity zone beneath Hawaii; the presence of hot asthenosphere is included; and the model also predicts upward movement of hot asthenospheric material several hundred kilometers downstream of the plume (which gives rise to secondary melting). The hot asthenosphere surrounding Hawaii effectively reduces the relative magnitude of the cylindrical low-velocity anomaly at 150 km depth, since the seismic inversion is sensitive only to relative variations across the modeled region. For these models, the magnitude of the recovered anomaly for the plume conduit is reduced by a factor of six for S waves and by a factor of eight for P waves. This example illustrates that it is unlikely that a plume conduit at Hawaii would be resolvable from the PELENET inversions.

6. Concluding discussion

Despite the limitations of the PELENET experiment due to the sparseness of the network, the results of the delay-time inversions yield important information about the pattern of seismic structure along the Hawaiian Islands. While the lack of a plume conduit imaged beneath the island of Hawaii may be explained by the poor resolution of such a feature (Fig. 6), the presence of low velocities beneath the region of Maui and Molokai is an unexpected discovery that is more difficult to interpret. Whereas the recovered velocity anomaly is 0.6% for P models and 1.8% for S models, resolution tests indicate that the magnitude of the anomaly could be two to three times larger, although this factor will also depend on the geometry of the unknown structure. Given that the delay-time data are not well fit by shallowly constrained models (Fig. 5), we can exclude the possibility that the low velocities reflect differences in lithospheric structure, such as erosion of the lower lithosphere beneath Maui and Molokai. The anomaly also cannot be explained by lithospheric differences associated with the offset in seafloor age across the Molokai Fracture Zone. We have modeled such an offset in lithospheric thermal structure with synthetic resolution tests and found that it would be both too small and too shallow to produce a resolvable effect.

We suggest that the Maui–Molokai anomaly may reflect a region of secondary melting downstream from the hotspot upwelling. Some melt should be present away from the location of the active hotspot: a stage of 'rejuvenated' volcanism (renewed volcanic activity occurring 0.25–2.5 Myr after the postshield-volcanism stage) is generally observed at Hawaiian volcanoes [31], although the timing and duration of this volcanism is var-

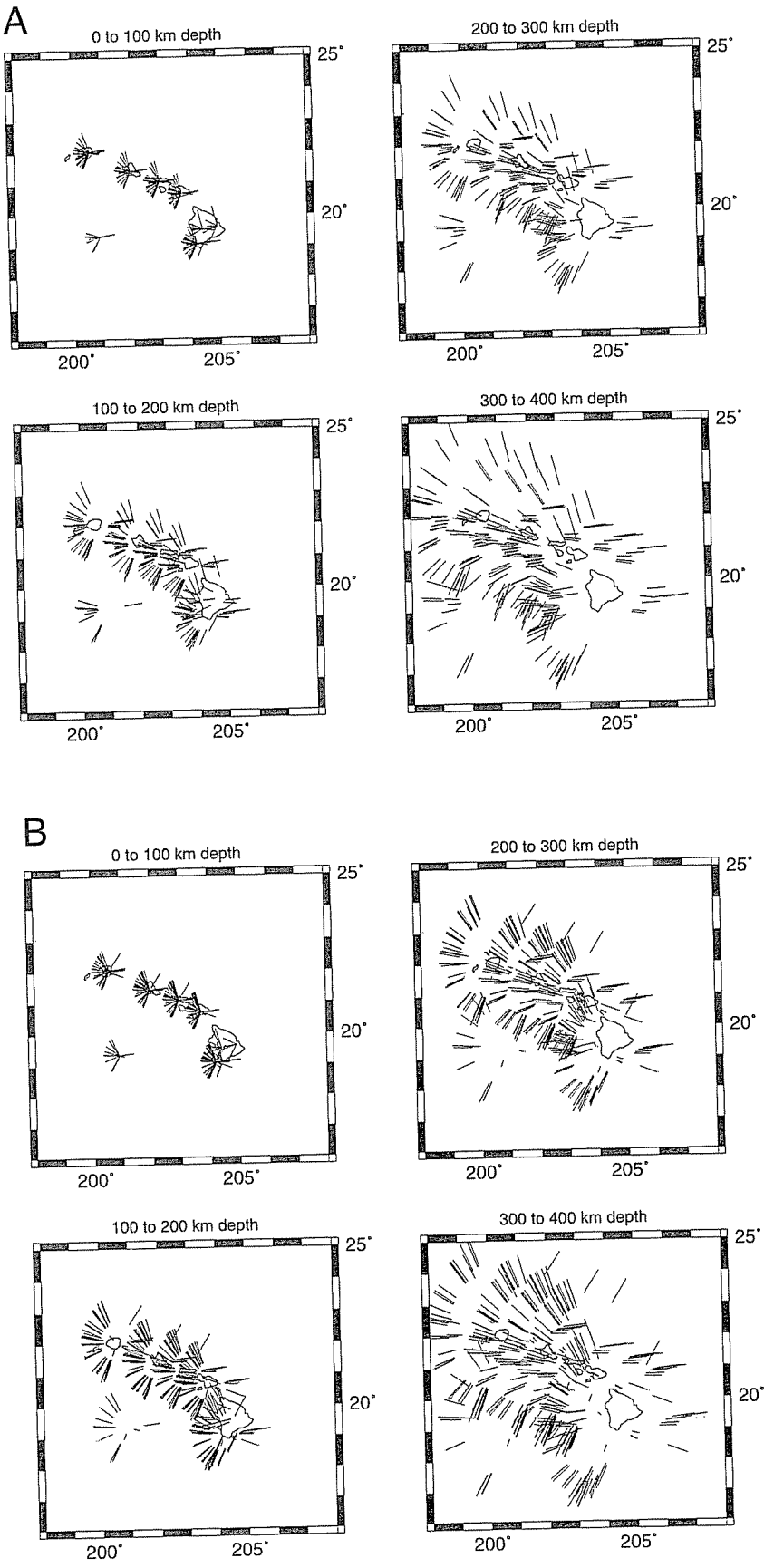
A
0 to 100 km depth
200 to 300 km depth
100 to 200 km depth
300 to 400 km depth
B
0 to 100 km depth
200 to 300 km depth
100 to 200 km depth
300 to 400 km depth
25°
20°
200°
205°

Fig. 6. The horizontal projection of the rays used for three-dimensional inversions in the depth intervals 0–100, 100–200, 200–300, and 300–400 km. (A) Distribution of rays for P waves. (B) Distribution of rays for S waves.
←

iable. Within the past 1 Myr, rejuvenated-type volcanism has occurred at all of the islands of Kauai, Oahu, Molokai, and Maui [31]. At present, the region of most active rejuvenated volcanism occurs at Maui, where the Haleakala volcano erupted ~200 years ago [32]. Bergmanis et al. [32] document 59 eruptions at the southwest rift zone of Haleakala within the past ~50 000 years, with a cumulative volume of ~2.4 km^3. The characteristics of rejuvenated-stage eruptions outside the southwest rift zone remain unknown, although Bergmanis et al. [32] speculate there has been a similar number of eruptions on the east rift zone of Haleakala. Within the past 1000 years, there have been at least six eruptions on the southwest rift zone, and six eruptions have also been mapped outside the southwest rift zone. Given these statistics, Haleakala is one of the most active volcanoes on the Hawaiian Islands in terms of the frequency of eruptions, surpassed only by Mauna Kea, Kilauea, and perhaps Loihi, where the eruptive frequency is unknown (John Sinton, personal communication, 2000).

A region of secondary melting is also plausible geodynamically. Such behavior is predicted in the models of Ribe and Christensen [6], who attribute the physical mechanism to a transition between two limiting flows: an axisymmetric flow near a rising cylindrical plume stagnating against a rigid lithosphere, and a 'thin-layer' flow farther downstream in which buoyant plume material spreads laterally and thins, moving material upward and generating melting. While Ribe and Christensen [6] predict that this secondary melting zone is located 300–500 km from the hotspot locus, a position in the vicinity of Kauai and beyond, the seismic images suggest that such a melting zone may instead be located closer to the hotspot.

Our tomographic images can be used to place bounds on the fraction of melt producing the Maui–Molokai anomaly. For melt residing in randomly oriented, film-like inclusions, the P- and S-velocity reduction, per percent melt, is 1.8% and 3.3%, respectively [33,34]. Given the results of our resolution tests showing that the Maui–Molokai velocity anomaly is reduced by a factor of two to three in our tomographic images, the percentage melt necessary to produce the observed anomalies is in the range 0.5–1% (P) and 1–1.5% (S).

The results from PELENET illustrate the ability of regional broadband seismic networks to provide new constraints on the pattern of upper mantle flow and melting beneath Hawaii. Because of the limited coverage of island locations, however, a more complete image of the mantle seismic structure beneath Hawaii will require the simultaneous deployment of ocean-bottom and land seismometers, in order to surround the hypothesized site of upwelling and to sample the core of the postulated conduit with crossing rays. Given the rate of earthquakes producing measurable P- and S-wave delays at the PELENET stations and on the OSNPE seafloor instrument, our study supports the viability of such a future land and ocean-bottom seismometer experiment to determine in three-dimensional detail the structure of the upper mantle beneath the Hawaiian hotspot.

Acknowledgements

We thank Randy and Adriana Kuehnel for their efforts in deploying and servicing the CIW seismometers, as well as several individuals who assisted with site selection, including Kunane Aipoalani, Dottie Bekeart, Mike Blackford, Solomon Kahalewai, Randy Lite, Derek Lee Loy, Martie and Don Nitcshe, Paul Okubo, Robert Serrano, and Mark Waterson. Emile Okal generously contributed to the deployment and operation of Northwestern University instruments, the Incorporated Research Institutions for Seismology provided data from GSN station KIP as well as the loan of spare PASSCAL disks and REFTEK recorders during the experiment. Suzan van der Lee graciously provided her code to correct for instrument responses. We thank Neil Ribe

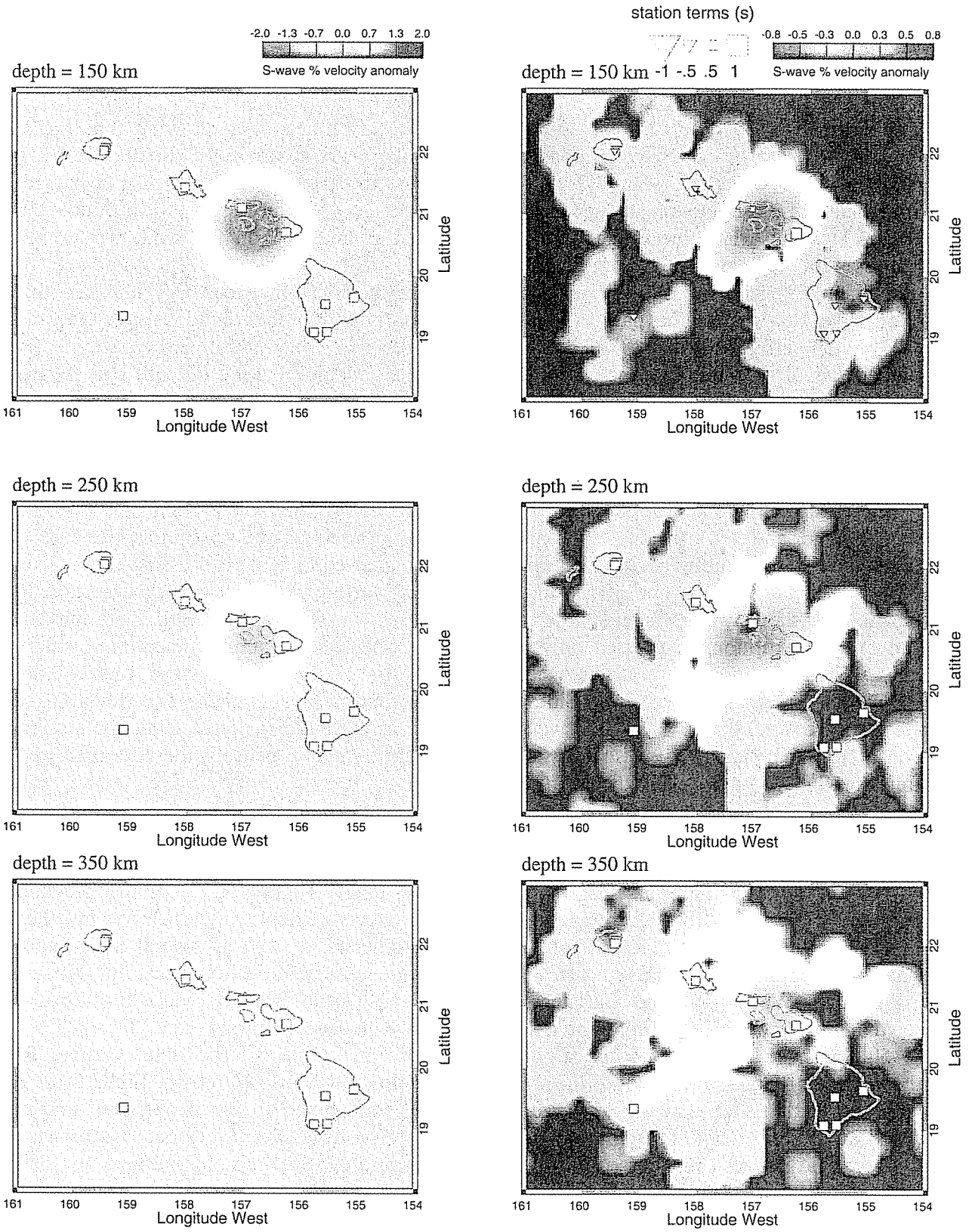

Fig. 7. Resolution test of a low-velocity anomaly at Maui and Molokai (see text) using the S-wave ray set. The synthetic input model is shown in the left column, and the results of inverting data calculated from this model, with 0.1-s rms Gaussian noise added, are shown in the right column. Note the difference in amplitude scales between the left and right columns. See Fig. 4 and text for further explanation.

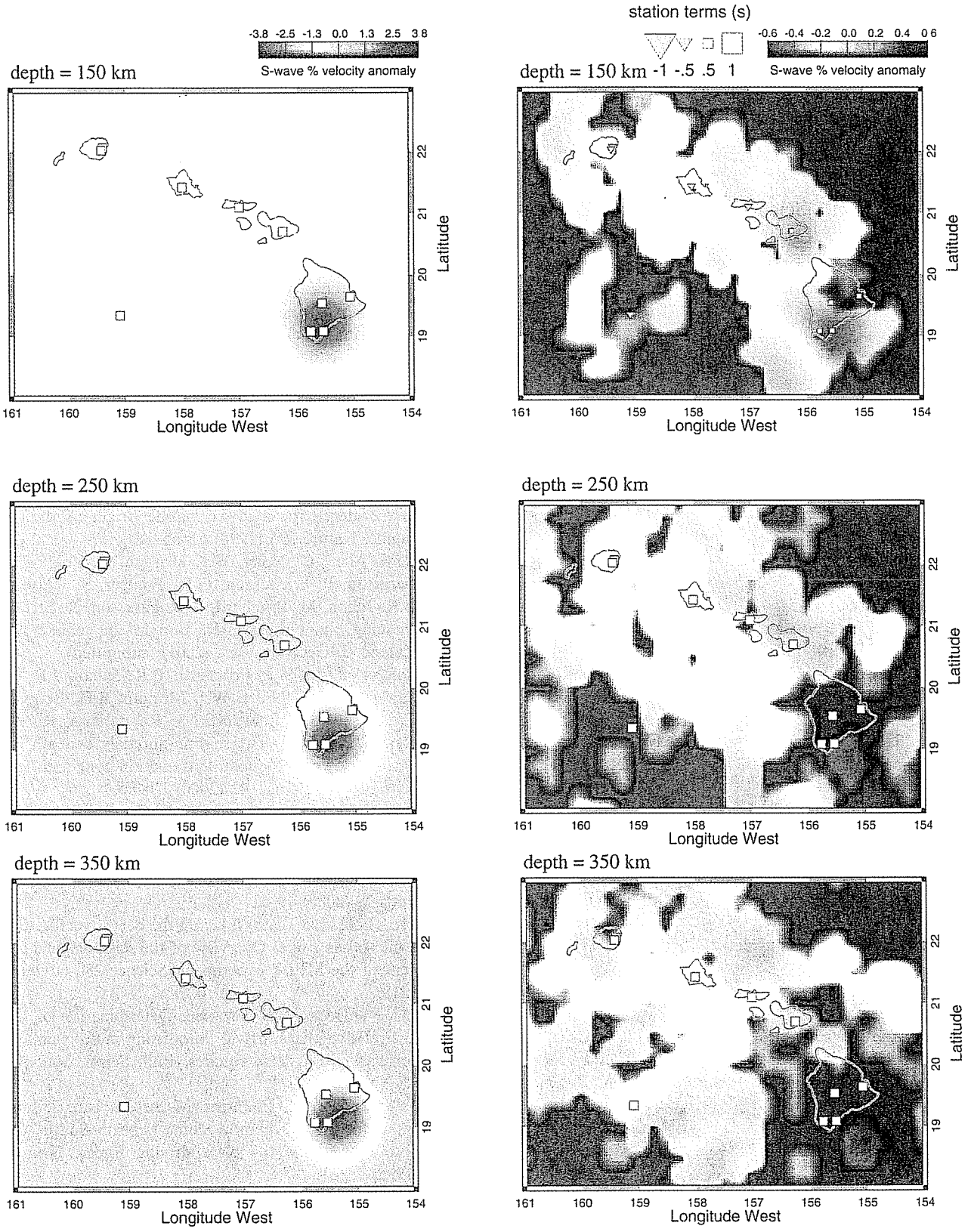

Fig. 8. Resolution test of a geodynamic model for the Hawaiian mantle plume using the S-wave ray set (see text), which indicates that PELENET data have poor resolution of a plume conduit located beneath southeastern Hawaii. The synthetic input model is shown in the left column, and the results of inverting data calculated from this model, with 0.1-s rms Gaussian noise added, are shown in the right column. Note the difference in amplitude scales between the left and right columns. See Fig. 4 and text for further explanation.

and Ulrich Christensen for providing their geodynamic model of Hawaii. Ken Dueker, Yang Shen, and an anonymous reviewer provided constructive comments that improved the manuscript. This work was supported by the National Science Foundation under Grants OCE-9618125 (C.J.W.) and OCE-9402991 (S.C.S.) School of Ocean and Earth Science and Technology, University of Hawaii, contribution number 5933. Hawaii Institute of Geophysics and Planetology contribution number 1198. *[SK]*

References

[1] R.S. Detrick, S.T. Crough, Island subsidence, hot spots, and lithospheric thinning, J. Geophys. Res. 83 (1978) 1236–1244.

[2] D.A. Yuen, L. Fleitout, Thinning of the lithosphere by small-scale convective destabilization, Nature 313 (1985) 125–128.

[3] P. Olson, Hot spots, swells, and mantle plumes, in: M.P. Ryan (Ed.), Magma Transport and Storage, Wiley, New York, 2000, pp. 33–51.

[4] N.H. Sleep, Hotspots and mantle plumes: Some phenomenology, J. Geophys. Res. 95 (1990) 6715–6736.

[5] N.M. Ribe, U.R. Christensen, Three-dimensional modeling of plume-lithosphere interactions, J. Geophys. Res. 99 (1994) 669–682.

[6] N.M. Ribe, U.R. Christensen, The dynamical origin of Hawaiian volcanism, Earth Planet. Sci. Lett. 171 (1999) 517–531.

[7] J. Phipps Morgan, W.J. Morgan, E. Price, Hotspot melting generated both hotspot volcanism and a hotspot swell?, J. Geophys. Res. 100 (1995) 8045–8062.

[8] S. Watson, D. McKenzie, Melt generation by plumes: A study of Hawaiian volcanism, J. Petrol. 32 (1991) 501–537.

[9] G.F. Davies, Ocean bathymetry and mantle convection. 1, Large-scale flow and hotspots, J. Geophys. Res. 93 (1988) 10,467–10,480.

[10] T.H. Jordan, Mineralogies, densities, and seismic velocities of garnet lherzolites and their geophysical implications, in: F.R. Boyd, H.A.A. Meyer (Eds.), The Mantle Sample: Inclusions in Kimberlites and Other Volcanics, AGU, Washington, DC, 1979, pp. 1–14.

[11] W.L. Ellsworth, R.Y. Koyanagi, Three-dimensional crust and mantle structure of Kilauea Volcano, Hawaii, J. Geophys. Res. 82 (1977) 5379–5394.

[12] F.J. Tilmann, H.M. Benz, K.F. Priestly, P.G. Okubo, P-wave velocity structure of the uppermost mantle beneath Hawaii from travel time tomography, Geophys. J. Int. 146 (2001) 594–606.

[13] M.T. Woods, E.A. Okal, Rayleigh-wave dispersion along the Hawaiian swell: A test of lithospheric thinning by thermal rejuvenation at a hotspot, Geophys. J. Int. 125 (1996) 325–339.

[14] K. Priestley, F. Tilmann, Shear-wave structure of the lithosphere above the Hawaiian hotspot from two-station Rayleigh wave phase velocity measurements, Geophys. Res. Lett. 26 (1999) 1493–1496.

[15] G. Laske, J. Phipps Morgan, J.A. Orcutt, First results from the Hawaiian SWELL pilot experiment, Geophys. Res. Lett. 26 (1999) 3397–3400.

[16] X. Li, R. Kind, K. Priestley, S.V. Sobolev, F. Tilmann, X. Yuan, M. Weber, Mapping the Hawaiian plume conduit with converted seismic waves, Nature 405 (2000) 938–941.

[17] I.Th. Bjarnason, C.J. Wolfe, S.C. Solomon, G. Gudmundson, Initial results from the ICEMELT experiment: body wave delay times and shear-wave splitting across Iceland, Geophys. Res. Lett. 23 (1996) 459–462; Correction, Geophys. Res. Lett. 23 (1996) 903.

[18] C.J. Wolfe, I.Th. Bjarnason, J.C. VanDecar, S.C. Solomon, Seismic structure of the Iceland mantle plume, Nature 385 (1997) 245–247.

[19] Y. Shen, S.C. Solomon, I.Th. Bjarnason, C.J. Wolfe, Seismic evidence for a lower mantle origin of the Iceland plume, Nature 395 (1998) 62–65.

[20] R.M. Allen, G. Nolet, W.J. Morgan, K. Vogfjord, B.H. Bergsson, P. Erlendsson, G.R. Foulger, S. Jakobsdottir, B.R. Julian, M. Pritchard, S. Ragnarsson, R. Stefansson, Imaging plume-ridge interaction in the mantle beneath Iceland, J. Geophys. Res. (2001) (submitted).

[21] G.R. Foulger, M.J. Pritchard, B.R. Julian, J.R. Evans, R.M. Allen, G. Nolet, W.J. Morgan, B.H. Bergsson, P. Erlendsson, S. Jakobsdóttir, S. Ragnarsson, R. Stefansson, K. Vogfjörd, The seismic anomaly beneath Iceland extends down to the mantle transition zone and no deeper, Geophys. J. Int. 142 (2000) F1–F5.

[22] J.A. Collins, F.L. Vernon, J.A. Orcutt, R.A. Stephen, K.R. Peal, F.B. Wooding, F.N. Spiess, J.A. Hildebrand, Broadband seismology in the oceans: Lessons from the Ocean Seismic Network Pilot Experiment, Geophys. Res. Lett. 28 (2000) 49–52.

[23] MELT Seismic Team, Imaging the deep structure beneath a mid-ocean ridge: Overview of the seismological component of the MELT experiment, Science 280 (1998) 1215–1218.

[24] J.C. VanDecar, R.S. Crosson, Determination of teleseismic relative phase arrival times using multi-channel cross correlation and least squares, Bull. Seism. Soc. Am. 80 (1990) 150–169.

[25] J.C. VanDecar, D.E. James, M. Assumpçao, Seismic evidence for a fossil mantle plume beneath South America and implications for plate driving forces, Nature 378 (1995) 25–31.

[26] S.C. Webb, Broadband seismology and noise under the ocean, Rev. Geophys. 36 (1998) 105–142.

[27] B.L.N. Kennett, E.R. Engdahl, Travel times for global earthquake location and phase identification, Geophys. J. Int. 105 (1991) 429–466.